DOI: 10.1111/mice.12548

ORIGINAL ARTICLE

COMPUTER-AIDED CIVIL AND INFRASTRUCTURE ENGINEERING WILEY

Hybrid physics-based modeling and data-driven method for diagnostics of masonry structures

Rebecca Napolitano | **Branko Glisic**

Department of Civil and Environmental Engineering, Princeton University, Princeton, NJ, USA

Correspondence
Rebecca Napolitano, Department of Civil and Environmental Engineering, Princeton University, Princeton, NJ 08544, USA.
Email: becca.napolitano@gmail.com

Funding information
National Science Foundation, Grant/Award Number: DGE-1656466

Abstract

Before implementing monitoring systems or reinforcements on a historic structure, it is essential to understand how crack patterns may have originated and how they affect the stability of the structure. Previous methods combining photogrammetry with physics-based modeling have been successful in diagnosing the cause of crack formation. However, a limitation of existing methods is the manual comparison process to ascertain damage origins. This research outlines a method combining physics-based modeling and data-driven approaches to automate diagnostics for existing masonry structures. This method was shown to quantitatively reproduce the cause of damage for complex, 3D structures and was validated against a laboratory-scale experimental masonry wall. The newly automated procedure increases throughput by 10^5 times compared to our prior method, allowing for the testing of orders of magnitude more hypotheses than were previously possible. Although the approach is demonstrated here for settlement-induced cracking, it has important implications for the broader topic of data-driven masonry diagnostics.

1 | INTRODUCTION

Research has shown that every year the United States alone demolishes 1 billion square feet of existing buildings and replaces them with new ones. From this constant stream of demolition and construction, nearly 43% of the materials end up in a landfill (Merlino, 2018). Thus, preservation and adaptive reuse of existing structures can not only protect world heritage, but can also serve as sustainable infrastructure solutions (Langston, 2010, 2012; Langston & Langston, 2008).

However, before existing structures can be preserved, retrofit, or reused, a thorough diagnostic assessment is vital. Diagnostics assessment synthesizes documentation (photogrammetry, laser scanning, and photographs), archival research, nondestructive evaluation (ground penetrating radar and thermal imaging), and physics-based modeling, to identify and quantify the extents of damage as well as ascertain their origins. By understanding the origins of damage on a structure, efficient monitoring and preservation plans can be implemented, as well as more accurate prognostics and calculations about service life can be made (Harris, 2001; Watt, 2009).

Although current practices, such as condition assessments and crack maps, can record the effects of stresses on a structure, they do not record causes. Taking into account only the structure's present condition, condition assessments alone cannot provide information about underlying catalysts of damage or predictive insights into a structure's potential for damage. For instance, damage on a structure could have already stabilized and not be related to current risks

(Taylor, 2005). To attain information regarding diagnostics and prognostics, existing damage patterns have been considered in combination with nondestructive testing and/or physics-based modeling.

Physics-based models can provide approximations of existing conditions (Anderson & Burnham, 2004). Thus, diagnostics has been commonly carried out by comparing existing conditions with the results of physics-based modeling. Lourenço (2002) used force-displacement diagrams to quantitatively compare the results of experimental testing and a multisurface interface model. A comparison of force-displacement diagrams was also used by Giordano, Mele, and De Luca (2002) to compare numerical curves for ABAQUS, CASTEM, and UDEC to experimental models. Subsequently, this technique has been successfully utilized by others for diagnostics of existing masonry structures (see Bui, Limam, Sarhosis, & Hjiaj, 2017; Fang, Napolitano, Michiels, & Adriaenssens, 2019; Giamundo, Sarhosis, Lignola, Sheng, & Manfredi, 2014; Najafgholipour, Maheri, & Lourenço, 2013; Sarhosis, Tsavdaridis, & Giannopoulos, 2014; Sarhosis, Garrity, & Sheng, 2015).

Another conventional means of diagnosing damage on an existing masonry structure is through a combination of nondestructive testing methods, structural health monitoring, and numerical modeling (Binda, Saisi, & Tiraboschi, 2000; Binda & Saisi, 2009; Bosiljkov, Uranjek, Žarnić, & Bokan-Bosiljkov, 2010; Gentile & Saisi, 2007; Russo, 2013; Shrestha et al., 2017). Anzani, Binda, Carpinteri, Invernizzi, and Lacidogna (2010) used this approach when they successfully combined pseudo-creep, sonic, and flat-jack tests, acoustic emission techniques, and finite element modeling to assess existing damage of historic masonry towers. In that work, quantitative comparisons were only drawn between the results of acoustic emission monitoring and the time of seismic events. Qualitative methods were used to compare the existing damage and the results of numerical modeling. A similar approach was used by Milani, Valente, and Alessandri (2017) when archival research, soil testing, laser scanning, and numerical modeling were used to diagnose existing cracks on the narthex of the Church of the Nativity in Bethlehem. This work comprehensively examined how existing damage could have arisen on the structure by qualitatively comparing the cracks on the existing structure to the results of a simulation. Qualitative comparison of existing crack patterns to the results of simulation is prevalent in the literature (Alessandri, Garutti, Mallardo, & Milani, 2015; Bayraktar, Altunişik, Sevim, & Türker, 2011; Douglas, Napolitano, Garlock, & Glisic, 2019; Michiels, Napolitano, Adriaenssens, & Glisic, 2017; Ramos & Lourenço, 2004; Wood et al., 2017).

Although the previously discussed works have outlined methods for comparing existing damage with the results of nondestructive testing and/or physics-based modeling, none of them considered more than one possible load case as the catalyst for damage. In reality, however, there are an infinite combination of causes, which could have caused the existing damage pattern. Although the approach in the previous literature is less time-consuming than an exhaustive exploration of all possible loading scenarios (infinite), the method of multiple working hypotheses (MMWH) provides a middle ground. Since it is not computationally possible to consider every possible loading combination for every structure, engineering judgment must be used in conjunction with background research on the structure to understand the appropriate hypotheses to test. This promotes divergent thinking and minimizes the adverse effects of diagnostic bias while still being computationally efficient.

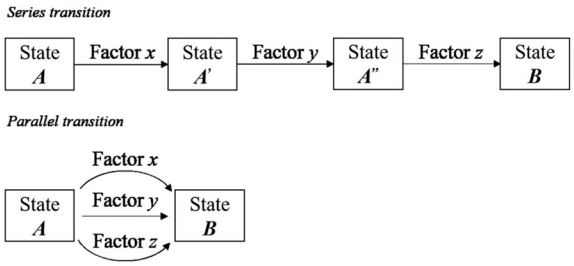

FIGURE 1 Diagram of MMWH showing the two types of changes in state (Adapted from Elliott & Brook, 2007)

1.1 | Method of multiple working hypotheses

As early as 1890, Thomas Chamberlin noted how the "dangers of parental affection for a favorite theory" could bias inductive reasoning (Chamberlin, 1992). To reduce the effects of diagnostic bias, Chamberlin advocated for the MMWH. In MMWH, a diagnostician develops a set of candidate models spanning the space of plausible damage scenarios; each model represents the movements from a single causative factor, which changes the state of the structure. Figure 1 depicts two types of changes in state: a series transition and a parallel transition. In the series transition, there are several intermediate states between A and B, which are caused by individual factors x, y, and z. In the parallel transition, there are no intermediate states between A and B; the change from A to B is the result of all concurrent factors. The parallel transition highlights a critical difference between MMWH and the development of alternative hypotheses: MMWH explicitly recognizes that more than one hypothesis may be true at the same time (Elliott & Brook, 2007). This is important for building diagnostics, where damage is often caused by multiple mechanisms.

1.2 | Current methods for selecting a model

A common adage about statistical models states "All models are wrong, but some are useful" (Box, 1979). If all models are wrong, a method of selecting the most useful model, or the

one that best represents the inference from the data, is vital when comparing multiple hypotheses (Burnham & Anderson, 2004). By definition, information-theory-based model selection attempts to (a) identify the model that best approximates the data and (b) order models from most affine to least (Anderson & Burnham, 2004; Burnham & Anderson, 2004).

Napolitano, Hess, Coe-Scharff, and Glisic (2019) examined how multiple finite-distinct element models could be compared to existing conditions to understand potential causes. Combinations of gravity and settlement were carried out in a preliminary investigation of a foundation wall in the Florence Baptistery. The results were qualitatively compared to the existing condition to understand if the results would be different enough to ascertain an affinity order. In addition, this method was also used to compare potential causes of damage in Palazzo Vecchio (Napolitano, Hess, & Glisic, 2019a) and Morris Island Lighthouse (Blyth, Napolitano, & Glisic, 2019).

This work was expanded upon in Napolitano and Glisic (2019a), where a method for diagnosing the most probable causes of cracks on existing structures was outlined. A result of this work was a statistical method that could be used to quantitatively compare the locations of bricks in a photogrammetry model and the locations of bricks in various physics-based simulations. The method was compared to the results of experimental testing and found to be successful. Subsequently, it was applied to further investigate the causes of damage in the foundation of the Florence Baptistery (Napolitano, Hess, & Glisic, 2019c).

There are several limitations of the method outlined in Napolitano and Glisic (2019a). Since the method is manual, the comparison of multiple cases is very time-consuming. If there are n joints in a structure, where a joint is the interface between two bricks, comparison with one load case requires n computations. However, comparison of the locations where cracking can occur with m load cases requires $m \times n$ computations. Thus, as the hypothesis space is expanded, the time can increase dramatically. Furthermore, since there is a considerable time penalty for including a variety of different loading conditions, this could allow diagnostic bias to be introduced to the analysis.

In addition to being time-intensive, the previous method was nonexhaustive. To limit the number of computations needed, a subsample of the total number of joints, j_s, at which crack width was compared was randomly chosen. One issue with that could be localized damage on a large structure. If a joint where there is displacement is not randomly selected, then the diagnosis will not include that damage. In this paper, a method is proposed that overcomes these limitations. Through automation of the comparison process, not only can the entirety of the structure, that is, every joint, be accounted for, but the time for multiple comparisons can also be dramatically reduced.

1.3 | Research aim and scope

This work aims to demonstrate the ability to correctly infer the cause of deformed (i.e., damaged) regions of masonry structures. In the current work, we limit the scope to settlement-induced deformations and focus on accurately inferring the parameters of the settlement event from a relatively sparse library of examples. We make the use of earth mover's distance (EMD) as a distance metric between these examples and Gaussian process regression (GPR) to perform interpolation on the resulting distances. Thus, while we make use of existing mathematical tools, the workflow combining them into a method for masonry diagnostics is novel. To our knowledge, this data-driven diagnostics approach has never before been applied to masonry structures. Therefore, the computational novelty in this work is an automated, quantitative method for diagnosing the causes of crack patterns in masonry structures by comparing the locations and magnitudes of cracks on an existing structure to a series of simulated crack patterns.

First, the method was tested on a simulated 3D structure, where the ground-truth damage cause was known. This enabled validation and profiling of the workflow performance. The method was then applied to an experimental (laboratory-scale) masonry wall with a diffuse crack pattern. In this case, the ground-truth damage was again known, but the positions and damage conditions had to be mapped from the physical wall to the simulations.

2 | METHODS

2.1 | Point cloud segmentation

For this work, we consider the point cloud P representing the surface of the damaged structure to be an input. P can be obtained by a variety of well-established methods that are described elsewhere (Barsanti, Remondino, Fenández-Palacios, & Visintini, 2014; Napolitano & Glisic, 2018; Patias et al., 2013). Commonly, when damage assessments are done, different damages are not separated out and attributed to individual causes (Binda, Gambarotta, Lagomarsino, & Modena, 1999; Napolitano, Hess, & Glisic, 2019b). In those cases, the results of diagnostics are heuristic. However, to optimize the time and money spent on preservation and monitoring efforts, it is more beneficial to be able to diagnose each damage individually. This is particularly important for older masonry structures, which have seen several damaging loading periods over their service life.

In the present method, segmentation is used to break the point cloud P, into distinct regions. This provides the twofold benefit of allowing each segment P_i to be analyzed independently and reducing the computational burden by reducing the $\mathcal{O}(N^3)$ optimal transport problem (where N is the number of points) into a $\mathcal{O}(n \times N_i^3)$ problem (where n is the number of

segments). The cubic complexity of optimal transport results in significant cost savings when $N_i < N$. From the segmentation, we produce a mapping $m(P) \rightarrow \{P_i\}$ (in this case, m is simply the list of indices for each point in each segment). This mapping is applied to each deformed geometry Q in the test library (described in Section 2.2) such that segments P_i and Q_i refer to the same region in space. Enforcing the mapping in this way requires a known correspondence between points in P and Q (in the case of one-to-one correspondence) or the use of bounding volumes such as alpha shapes (when one-to-one is not guaranteed). In this work, we obtain the correspondence using the Hungarian algorithm since we composed P and Q from brick centroids with the same number of bricks.

We apply Mini-Batch K-Means (MBKM) (Béjar Alonso, 2013) to generate the segmentation mapping m, with the only input parameter being the number of segments n. Since the purpose of the segmentation is strictly to provide independent diagnostics for different regions of the structure, the particular choice of segments is driven by the user's preference (i.e., which segmentation will provide the most helpful information). The number of neighbors for MBKM is left to the readers' engineering judgment. A study illustrating the sensitivity to segmentation has been included in Section 3.1.1. This provides a convenient way to group compact portions of the point cloud together. In our testing, we found the workflow to be robust to the particular choice of segmentation, including the number of segments and algorithm applied. Therefore, any other clustering technique or manual point selection (e.g., user-specified bounding boxes) should be equivalent in practice.

2.2 | Physics-based modeling

Distinct element modeling (DEM), a method of discontinuous structural analysis, was used for the physics-based modeling since it has been applied successfully in previous masonry research (Giordano et al., 2002; Kavanaugh, Morris, Napolitano, & Jorquera-Lucerga, 2017; Lemos, 1998; Lemos, 2007, 2019; Napolitano & Glisic, 2019b; Napolitano, Lansing, & Glisic, 2019; Papantonopoulos, Psycharis, Papastamatiou, Lemos, & Mouzakis, 2002). 3DEC, a distinct element modeling software package (Cundall & Hart, 2015), was used to simulate the masonry elements as rigid bodies. As cracking at the joints frequently dominates fracturing of the individual brick elements, this is an acceptable approximation (Asteris et al., 2015). The details of the numerical model and material properties can be found in (Napolitano & Glisic, 2019a).

For this work, we used a postulated undamaged state U (in the form of a triangulated mesh) and parameterized damage conditions c as inputs to the DEM simulation. The DEM simulation can then be thought of as a function S, which returns a deformed state Q according to the transformation $S(U; c) \rightarrow Q$. Each state Q, therefore, corresponds to the state P, and should be expected to be in given the damage condition c. By comparing each hypothesized damaged structure described by Q to the observed damaged structure described by P, we hope to identify the true damage c°, which affected the masonry structure. As aforementioned, since it is not computationally possible to hypothesize every possible loading combination, engineering judgment must be used in conjunction with background research on the structure to understand the appropriate hypotheses to test.

2.3 | Distance metric

To create a quantitative correspondence between P and Q (i.e., to decide how well each hypothesis matches the observed facts), we must define a distance metric that acts on point clouds. We use the EMD, which is a measure of the distance between two probability distributions and is proportional to the minimum amount of work required to transform one distribution into the other (Lupu, Selios, & Warner, 2017; Rubner, Tomasi, & Guibas, 2000; Yilmaz, 2009). In this case, EMD is the cost associated with the optimal transport of points between two point clouds (i.e., two discrete distributions in 3D space). To make this even more concrete, we remark that the distance $d(P, Q) = \text{EMD}(P, Q)$ has units of length, describing the total distance required to move the points in P through space to exactly align with Q. We utilize the Python Optimal Transport library to perform the calculation (Flamary & Courty, 2017).

2.4 | Interpolation between observations

Although the EMD metric provides a quantitative way to evaluate individual hypotheses, it becomes computationally intractable to identify the perfect value for c when damage conditions are parameterized in continuous space. Instead, we generate a library of hypotheses $\{(Q; c)_\ell\}$ and evaluate the distance between the existing conditions and every hypothesized structure, $d(P, Q_\ell)$. Because each Q_ℓ is paired with a c_ℓ and P with c°, these distances can now be considered a proxy for the otherwise unknown $d(c^\circ, c_\ell)$. We, therefore, apply GPR to approximate this distance field (Williams & Rasmussen, 1996). GPR is a Bayesian method for model selection and updating commonly used in the literature. Zhou, Yan, and Ou (2013) used GPR to calculate the relationship between design parameters and response characteristics of cable-stayed bridges. Xia and Tang (2013) used GPR to characterize the dynamic response of structures with high levels of uncertainty. Additionally, Wan and Ren (2014) used GPR and finite element analysis for model updating and parameter selection to ascertain uncertainty bounds for existing structures. In the current work, GPR effectively provides an interpolation of $d(c^\circ, c)$ to enable continuously varying c from the discrete set of c_ℓ in the library.

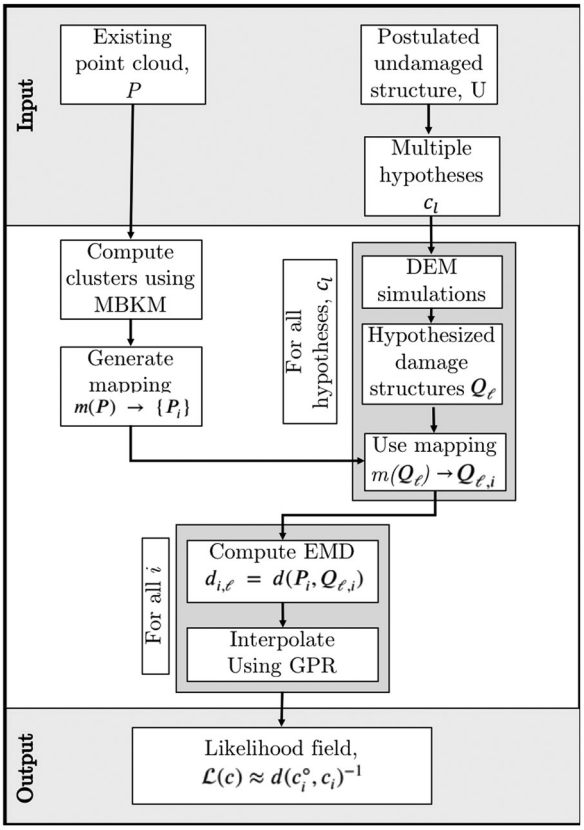

FIGURE 2 Work flow summarizing the method used in this paper

In practice, we interpolate $\mathcal{L} = d^{-1}$ to weight the model more strongly in regions where the distance is low (i.e., the guess is good) compared to regions where the distance is high. The result of this inversion is that the field estimated by GPR corresponds to the likelihood of c being the true damage condition, measured in units of m^{-1}. For instance, a value of 10 m^{-1} indicates a 10× less precise match compared to a value of 100 m^{-1}, since the optimal transport costs 0.1 m in the first case compared to 0.01 m in the second case.

2.5 | Summary of the method

We have integrated the procedures introduced above into a single workflow (Figure 2) for diagnosing crack patterns on masonry structures, which we summarize here. A point cloud P representing an existing, damaged structure is first acquired. Based on knowledge of the structure and possible damage patterns ascertained through archival research, a postulated undamaged state is generated in the form of a triangulated mesh U (e.g., manually using computer aided design [CAD]). Then, a library of hypothesized damaged structures $\{Q_\ell\}$ is generated by applying hypothesized damage conditions $\{c_\ell\}$ using DEM simulation, acting as $S(U; c_\ell) \rightarrow Q_\ell$. Using MBKM clustering, P is segmented into discrete sections and a mapping $m(P) \rightarrow \{P_i\}$ is generated. This mapping is applied to each Q_ℓ to generate segments $\{Q_{\ell,i}\}$, which are used to compute distances $d_{i,\ell} = d(P_i, Q_{\ell,i})$. For each segment i (or for any combination thereof), the inferred likelihood field $\mathcal{L}(c) \approx d(c_i^\circ, c_i)^{-1}$ is estimated by GPR. Thus, while our prior methodology required a comparison of individual hypotheses, the proposed approach provides an estimate for the likelihood of every possible hypothesis allowed by the given parameterization of the damage conditions (and within some reasonable range compared to hypotheses in the library).

3 | RESULTS AND DISCUSSION

3.1 | Application to synthetic test case

We first demonstrate the method on the synthetic structure shown in Figure 3. The use of synthetic data, where the ground-truth damage condition c° is known, is necessary to establish the accuracy of the method. We obtained a damaged structure P ($N = 9{,}633$ discrete elements), depicted in Figure 4, by simulating the deformation of the masonry structure under two settlement loads. One settlement load occurs at the location $(x, y) = (1.63, -1.73)$

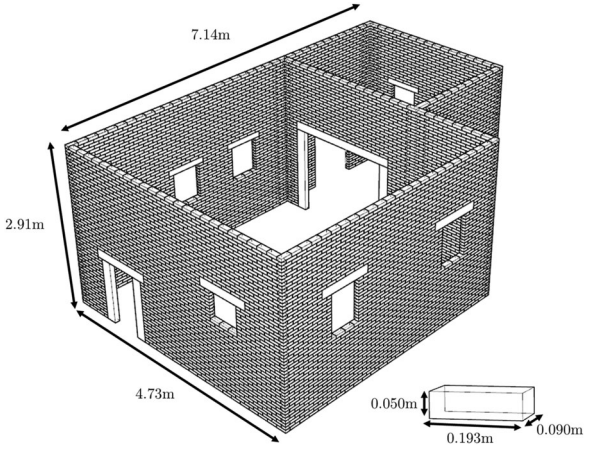

FIGURE 3 Geometry of synthetic masonry structure, including individual brick dimensions

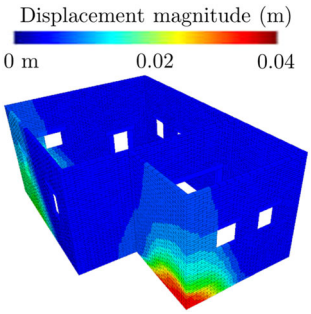

FIGURE 4 Displacement magnitude of each brick in the synthetic structure due to two different settlement events

with an amplitude $a = 0.157$ m; the amplitude refers to the depth of the settlement, which is the maximum of the Gaussian kernel. A second occurs at $(0.62, 3.22)$ with an amplitude of 0.160 m. In both cases, the settlement was imposed as a Gaussian kernel with dispersion $\sigma = 0.5$ m. We parameterize the ground-truth damage condition as $c^\circ = (1.63, -1.73, 0.157), (0.62, 3.22, 0.160)$. Note that the two independent damage events demonstrate the applicability of the method to multiple c°.

We generated a library of 256 Q_ℓ by selecting c_ℓ from a uniform random distribution on the domain $x \in [-0.39, 4.94]$, $y \in [-2.80, 5.13]$, and $a \in [0.00, 0.30]$. These again were imposed as a Gaussian kernel with dispersion $\sigma = 0.5$ m. Note that each hypothesis included only a single settlement event, in contrast to the ground-truth, which was constructed from multiple. We first computed the EMD between the full point clouds as $d(P, Q_\ell)$ without segmentation and generated a continuous estimate of the likelihood field by applying GPR to the inverted distances.

The results of the full point cloud comparison are illustrated in Figure 5. Since the likelihood field is a continuous quantity in (x, y, a), we have rendered the values of the field at five discrete points in a. The brighter values (yellow) correspond to (x, y) settlement centers, which most probably caused the damages on the target structure; the ground-truth damage conditions are illustrated as black crosses. Note the two distinct bright areas, which indicate that settlement is most likely to have occurred there; the results of the likelihood map qualitatively correspond to the true conditions. In this case, the highest likelihood of 68.7 m^{-1} is obtained at the location $c = (0.51, 3.28, 0.198)$, which roughly corresponds to the second settlement event, albeit at a larger amplitude. This compares to the 58.6 m^{-1} and 64.6 m^{-1} for the two true settlement events, and an average field value of 33.3 m^{-1}. In other words, the estimate from the GPR is that the true damage conditions are about twice as likely compared to the average over the investigated range. Thus, despite good qualitative agreement, the result is relatively weak.

To produce a direct comparison between the multiple-settlement ground-truth and the single settlement library,

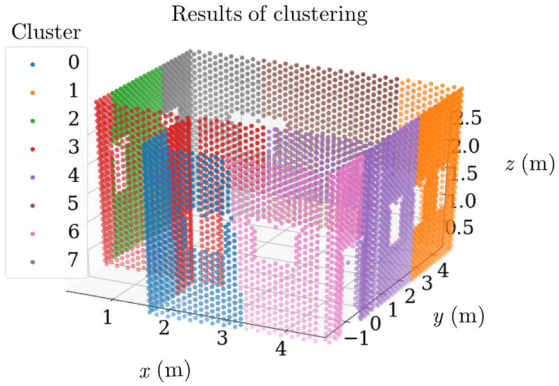

FIGURE 6 Segmented point cloud for 3D structure

we segmented the structure into eight segments (shown in Figure 6) using MBKM. As discussed above, the choice of $n = 8$ is driven purely by engineering judgment and does not substantially affect the analysis; an analysis of the effect of different segmentation is presented later in Section 3.1.1. We applied the selected segment mapping m to each of the 256 Q as described and calculated the discrete distances $d(P, Q_\ell)$ and thus the resulting likelihood fields correspond to only a single segment of the original geometry.

The likelihood field for Segment 0 only (blue in Figure 6), corresponding to the segment directly over the first settlement event, is shown in Figure 7. The most likely cause of settlement occurs at $(1.79, -1.65, 0.156)$ with a magnitude of 575 m^{-1}, compared to the true value $c = (1.63, -1.73, 0.157)$ (indicated by the black cross) with a magnitude of 558 m^{-1}, and the average likelihood of 105m^{-1}. As indicated by the visual representation of the likelihood field, this means the true value lies within a highly localized region of high intensity. The amplitude is highly confined to the $a = 0.15$ slice, but there is a somewhat diffuse pattern in the (x, y) plane. It is essentially bounded by potential encounters with other walls, which would provide counterexamples to this case which did not settle along the other walls in the small room.

Similarly, the likelihood field for Segment 7 only (gray in Figure 6), corresponding to the segment directly over the second settlement event, is shown in Figure 8. The most

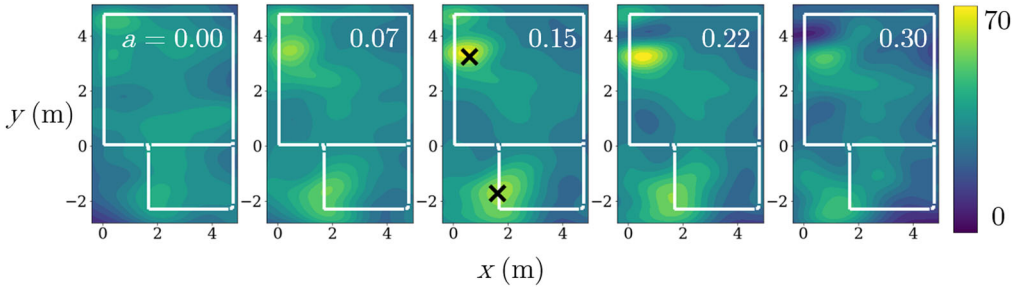

FIGURE 5 Estimate of the likelihood field $\mathcal{L}(c)$ obtained from full point cloud P. Field rendered over (x, y) slices for discrete amplitudes a as listed in each panel. Yellow color (lightest) indicates greater likelihood (in units of m^{-1}). Black crosses indicate the two components of c°. White lines are centroids of bricks to illustrate the position of the structure relative to the position of settlement centers

likely cause of settlement occurs at $(0.67, 3.28, 0.204)$ with a magnitude of 723 m^{-1}, compared to the true value $c = (0.62, 3.22, 0.160)$ (indicated by the black cross) with a magnitude of 679 m^{-1}, and the average likelihood of 94 m^{-1}. In this case, the localization is stronger in the $x - y$ plane and weaker in the direction of a, which can be seen in the bright yellow spot at $a = 0.22$. It is interesting to note that this probably arises from the fact that the settlement does not occur directly under the wall, so it in fact may be completely equivalent for a certain set of (x, a) pairs: distance from the wall increases along with the depth, the settlement felt by the wall remains constant.

3.1.1 | Sensitivity to segmentation

To quantify the effect of different segmentations on the results of the analysis, we perform segmentation with MBKM using five random seeds at each of $n = 7$, $n = 8$, and $n = 9$ (for a total of 15 segmentations, Figure 9). Although the peak likelihood values reported do appear to exhibit some variation, recall that these typically exist in the center of a cloud of highly likely conditions. Furthermore, these damage conditions correspond to fairly diffuse settlements and as such exhibit intrinsic degeneracy to the effective settlement experienced by each wall (i.e., multiple conditions may result in nearly identical settlement). We, therefore, conclude that the results are relatively insensitive to the particular choice of segmentation.

3.1.2 | Sensitivity to noise

A major concern with the use of this synthetic data set is the lack of noise introduced from point cloud acquisition. In a real system, measurement noise on the order of mm is introduced. To quantify the effect of such noise on our results, we artificially applied random noise to every point in P from a uniform distribution over $[-\delta, +\delta]$ in each of (x, y, z). We then repeated the analysis for Segment 7 (i.e., P_7) as described above. For each value of δ, we recorded the Z-score, $z = (\mathcal{L}(c^\circ) - \mu)/\sigma$, where μ and σ are the mean and standard deviation of $\mathcal{L}(c)$ over all c in the investigated range. This indicates the predicted significance of the true value c° compared to the background. We also measured error in predicted value as the Euclidean distance between the location of peak likelihood and c°.

The selected metrics are reported in Figure 10 as a function of δ over three decades. As expected, introducing noise to the point cloud decreases the Z-score for the true value and increases the prediction error. Unsurprisingly, $\delta = 0.1$ m seems to be untenable compared to model dimensions on the order of 5 m. However, it is encouraging to see that for the magnitude of noise expected from typical point cloud acquisition methods (on the order of 10^{-3} m), the method is quite robust. In fact, the error did not increase between 10^{-4} m and 10^{-3} m in our test case.

Using DEM, each brick in the simulation needs to be modeled individually. After creating the postulated undamaged structure, U, the centroids and/or vertices of each brick can be extracted. This work illustrated how the method would perform under the minimum required conditions. A user could additionally consider each vertex instead of the centroid to increase the density of the point cloud.

3.1.3 | Sensitivity to library size

We also performed a sensitivity study to understand the effects of data volume supplied to the GPR. As aforementioned, while the EMD metric provides a quantitative way to evaluate individual hypotheses, it becomes computationally intractable to identify the perfect value for c when damage conditions are parameterized in continuous space. Thus, we generated a library of hypotheses $\{(Q; c)_\ell\}$ so that we can evaluate the distance between the existing one and every hypothesized structure, $d(P, Q_\ell)$. The number of simulations was randomly down-selected from the original 256 generated for Section 3.1 to measure the performance with different library sizes. Again, we measure the error between peak likelihood and true value and report the result as a function of library size in Figure 11.

As the number of simulations in the library increases, the interpolation results improve, and thus the error in the prediction declines. These results show that while an increase in the number of simulations can reduce the distance to the ground-truth value, the median return-on-investment declines and the variance of data points stabilizes after

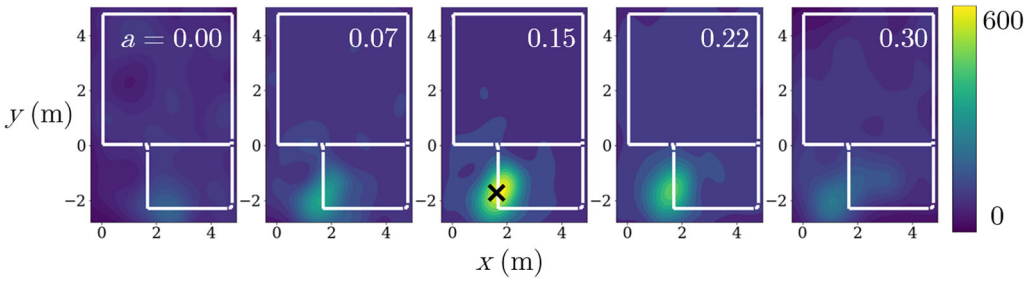

FIGURE 7 Estimate of the likelihood field $\mathcal{L}(c)$ obtained from P_0. Details otherwise same as Figure 5

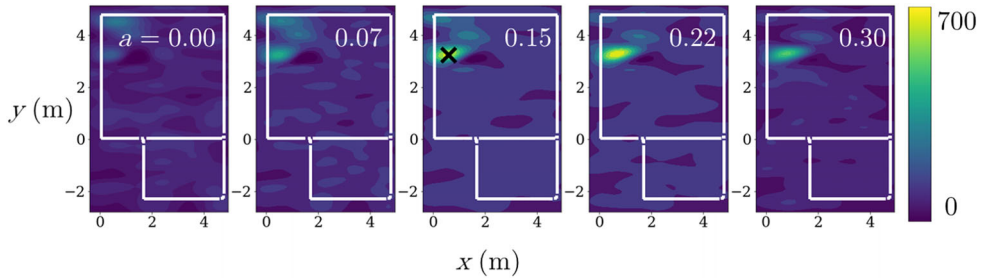

FIGURE 8 Estimate of the likelihood field $\mathcal{L}(c)$ obtained from P_7. Details otherwise same as Figure 5

$n = 7$	$n = 8$	$n = 9$
μ = (1.79, -1.67, 0.161); 560	μ = (1.80, -1.63, 0.156); 515	μ = (1.75, -1.70, 0.162); 464
σ = (0.08, 0.08, 0.009); 59	σ = (0.08, 0.08, 0.004); 136	σ = (0.09, 0.08, 0.000); 126
(1.69, -1.74, 0.156); 448	(1.69, -1.74, 0.162); 441	(1.85, -1.65, 0.162); 605
(1.90, -1.65, 0.174); 632	(1.79, -1.65, 0.156); 547	(1.63, -1.83, 0.162); 396
(1.74, -1.74, 0.162); 412	(1.90, -1.56, 0.150); 462	(1.69, -1.74, 0.162); 286
(1.79, -1.65, 0.150); 745	(1.79, -1.65, 0.156); 745	(1.79, -1.65, 0.162); 543
(1.85, -1.56, 0.162); 561	(1.85, -1.56, 0.156); 561	(1.79, -1.65, 0.162); 492

FIGURE 9 Representation of different segmentations resulting from MBKM with different n and random seed. Reported mean μ and standard deviation σ are for the given n. Each instance is reported with its maximum likelihood (x, y, a) and likelihood magnitude

approximately 100 simulations for this particular case. Note that the convergence near 256 arises from the sampling protocol (down-selecting from the original library), rather than anything unusual about that library size.

3.2 | Validation with experimental case

We also applied our method to a laboratory-scale experimental case study from our prior work to validate the method on a real (physical) structure. For an in-depth discussion of the experiment, see Napolitano and Glisic (2019a); in this work, only the pertinent aspects of the experiment have been distilled and summarized. A single-leaf, dry-joint masonry test wall was constructed on a base consisting of cinder blocks and a manual jack. Orthorectified photographs were used to capture the centroids of each brick after cracking to acquire P. The corner of the wall was settled to a depth of 0.021 ± 0.0001 m for a width of 2× brick length to induce a

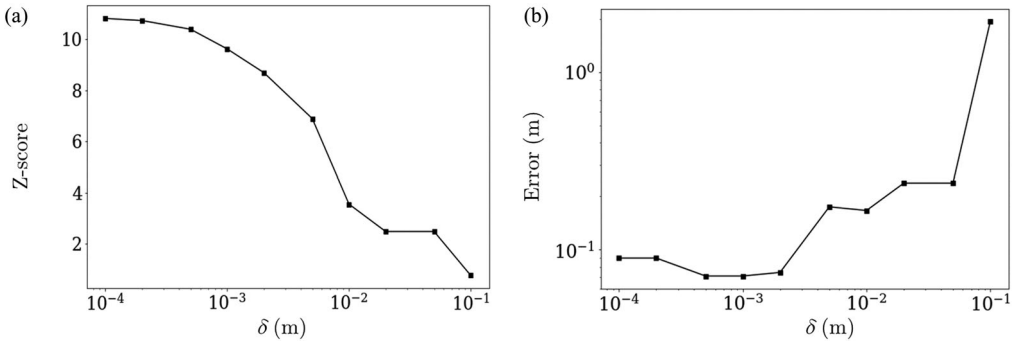

FIGURE 10 Effects of noise magnitude δ on (a) the Z-score and (b) error between peak likelihood and true value

long-range displacement event. The depth of settlement was determined by the depth at which cracking was evident; it was not carried further to avoid complete failure of the wall. The bricks have dimensions of $193 \times 55 \times 90 \pm 1$ mm (as indicated in Figure 12) and a density of $2{,}508.67 \pm 10$ kg/m^2.

As with the simulated data in the preceding section, the true damage condition c° is known, but is not utilized in generating the prediction. The undamaged structure is represented by a uniform wall of identical bricks (such assumptions would typically be made in generating U with CAD). We then produce the simulation library by varying the settlement center x, settlement width w, and settlement amplitude a. Thus, the damage condition is $c^\circ = (1.25, 0.39, 0.021)$. In this case study, we do not utilize segmentation since there are a small number of bricks ($N = 93$).

The likelihood field for damage on the entire wall is illustrated in Figure 13. The condition predicted from the peak likelihood is settlement at $(1.25, 0.44, 0.022)$ (magnitude $\mathcal{L} = 163$ m^{-1}) compared to the true value of $c^\circ = (1.25, 0.39, 0.021)$ (magnitude $\mathcal{L} = 157$ m^{-1}) and an average value of $\mathcal{L} = 72$ m^{-1}. Note that the prediction of $w = 0.44$ m is nearly identical to the true $w = 0.39$ m in practice because only integer number of bricks are settled. This result illustrates that the method can accurately determine the cause of damage, even when making assumptions about the structure of the undamaged wall (e.g., identical bricks in U) and introducing noise from the point cloud acquisition through orthorectified photographs.

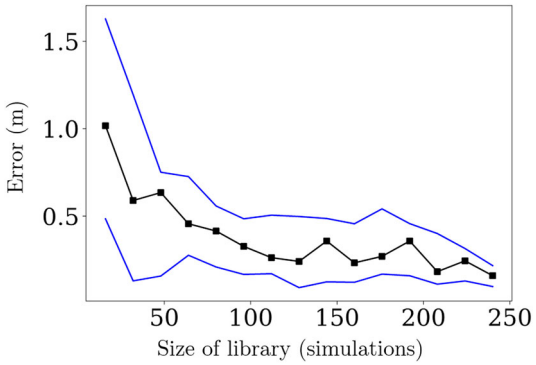

FIGURE 11 Effects of the library size (in number of simulations) on the error between peak likelihood and true value. Black line with squares on it indicates median value, while upper and lower blue lines indicate 75th and 25th percentiles, respectively (from 10 samples at each size)

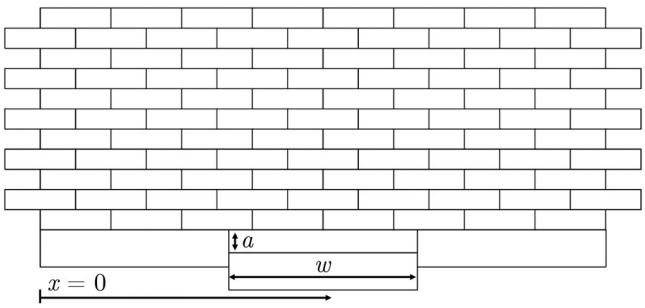

FIGURE 12 Geometry and definition of variables used in experimental setup

3.3 | Comparison to previous method

As discussed, the main limitation of the statistical method outlined in Napolitano and Glisic (2019a) is the amount of time required for comparison since the process is manual. In the previous work, the difference between the existing conditions and the numerical simulations (fractional distance) was computed on a subset of the total joints. The equations for calculating fractional distance and the subset of joints can be found in Napolitano and Glisic (2019a). Fractional distances were then manually compared between the existing conditions and five hypothesized simulations (requiring about 20 min of manual effort, or 240 s per hypothesis). The hypothesized simulation with the smallest fractional distance was selected to be the most probable cause of the existing damage on the structure.

With the present method, the experimental wall was compared to a library of 256 possible cases in 0.25 s, or 10^{-3} s per hypothesis on desktop PC with 32.0 GB of RAM and an Intel Core i7-770K CPU @4.20zGHz (for completeness, the synthetic wall took 83 s). Even without the newly developed interpolation capabilities, this represents an

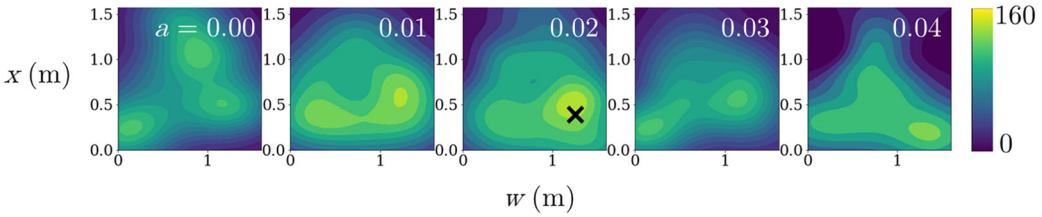

FIGURE 13 Estimate of the likelihood field $\mathcal{L}(c)$ obtained from the experimental wall. Details otherwise same as Figure 5

increase in throughput on the order of $10^5\times$ since it required 10^{-3} s per hypothesis and the previous method required 240 s per hypothesis. Additionally, the manual method did not allow for separation of damage patterns (i.e., segmentation) and thus delivered only a heuristic diagnosis, whereas the present method provides much more detailed information. In addition, the data-driven GPR approach enables a smooth interpolation in the parameter space, allowing for the possibility of hypotheses not present in the library.

4 | CONCLUSIONS

This paper outlines a method for diagnosing existing crack patterns on masonry structures, which introduces a hybrid physics-based modeling and data-driven approach. In particular, DEM is used to simulate the response of several masonry structures under diverse loading conditions, MBKM is used to segment regions of the existing and simulated point clouds, EMD is used to compare existing and simulated point clouds, and GPR is used to interpolate between those results. The method was validated against the results of a synthetic 3D structure with known ground-truth damage conditions. It was successfully able to interpolate from a library of prior examples to find the two independent causes of damage in different regions of the structure.

In addition, the method was validated using a case study based on prior laboratory-scale experimental testing. A diffuse cracking pattern was induced on the experimental wall, and the method was shown to be capable of quantitatively diagnosing the cause of damage. Several sensitivity studies were conducted to show robust handling of noise in the input point clouds, insensitivity to a particular choice of segments, as well as effect of reducing volume of prior examples. To understand how this new method compared to state-of-the-art methods in the field, it was directly compared for the experimental wall. Compared to our prior approach, this technique is on the order of $10^5\times$ faster and requires far less human intervention. This not only improves throughput, but also reduces diagnostic bias by including far more hypotheses in the evaluated set. Therefore, the computational novelty of this research is an automated, quantitative method for diagnosing the causes of crack patterns in masonry structures.

There are a few notable limitations of the present technique. First, point cloud acquisition from the exterior is not sufficient for "real" masonry structures consisting of multiple layers of material. Additional assumptions must then be made for the structure of the interior to arrive at a suitable U. This may be addressed in the future by the inclusion of an ensemble of $\{U_\ell\}$, which could be included as a parameter to test by the distance calculations.

The success of GPR interpolation requires that $\mathcal{L}$ be relatively smooth, which implies that the damage conditions c must be amenable to parameterization. Furthermore, generation of a suitable simulation library becomes difficult for high-dimensional c. That is, when many damage conditions are possible and the ranges cannot be easily bounded, much simulation effort may be wasted in regions with very low likelihood. Ideally, engineering judgment would be used to restrict parameter ranges when possible and separate damage into independent events, such as how two settlements events were predicted from a library of only single-settlement events in Section 3.1.

ACKNOWLEDGMENTS

This paper is based on work in part supported by the National Science Foundation Graduate Research Fellowship Program under Grant no. DGE-1656466. Any opinions, findings, and conclusions or recommendations expressed in this material are those of the authors and do not necessarily reflect the view of the National Science Foundation. Additional support was provided by the Dean's Fund for Innovation at Princeton and the Department of Civil and Environmental Engineering. The present research was completed as part of the Itasca Educational Partnership under the mentorship of Dr. Jim Hazzard. Many thanks to Wesley Reinhart for fruitful discussions.

AUTHOR CONTRIBUTIONS

Rebecca Napolitano carried out the experimental testing, simulations, analysis, and writing of this project. Branko Glisic guided the project in terms of direction and editing.

CONFLICT OF INTERESTS

The authors declare no potential conflict of interests.

REFERENCES

Alessandri, C., Garutti, M., Mallardo, V., & Milani, G. (2015). Crack patterns induced by foundation settlements: Integrated analysis on a Renaissance masonry palace in Italy. *International Journal of Architectural Heritage*, *9*(2), 111–129.

Anderson, D., & Burnham, K. (2004). *Model selection and multi-model inference* (2nd ed.). New York: Springer-Verlag.

Anzani, A., Binda, L., Carpinteri, A., Invernizzi, S., & Lacidogna, G. (2010). A multilevel approach for the damage assessment of historic masonry towers. *Journal of Cultural Heritage*, *11*(4), 459–470.

Asteris, P. G., Sarhosis, V., Mohebkhah, A., Plevris, V., Papaloizou, L., Komodromos, P., & Lemos, J. V. (2015). Numerical modeling of historic masonry structures. In P. G. Asteris, & V. Plevris (Eds.), *Handbook of research on seismic assessment and rehabilitation of historic structures* (pp. 213–256). Pennsylvania: IGI Global.

Barsanti, S. G., Remondino, F., Fenández-Palacios, B. J., & Visintini, D. (2014). Critical factors and guidelines for 3D surveying and modelling in cultural heritage. *International Journal of Heritage in the Digital Era*, *3*(1), 141–158.

Bayraktar, A., Altunişik, A. C., Sevim, B., & Türker, T. (2011). Seismic response of a historical masonry minaret using a finite element model updated with operational modal testing. *Journal of Vibration and Control*, *17*(1), 129–149.

Béjar Alonso, J. (2013). *K-means vs mini batch k-means: A comparison* (Technical Report). Universitat Poiltecnica de Catalunya, Barcelona Tech.

Binda, L., Gambarotta, L., Lagomarsino, S., & Modena, C. (1999). A multilevel approach to the damage assessment and seismic improvement of masonry buildings in Italy. In A. Bernardini (Ed.), *Seismic damage to masonry buildings* (pp. 170–195). Rotterdam: Balkema.

Binda, L., & Saisi, A. (2009). Application of NDTs to the diagnosis of historic structures. In O. Abraha and X. Derobert (Eds.), *7th International Symposium on Nondestructive Testing in Civil Engineering*, Nantes, France, June 30–July 3, 2009.

Binda, L., Saisi, A., & Tiraboschi, C. (2000). Investigation procedures for the diagnosis of historic masonries. *Construction and Building Materials*, *14*(4), 199–233.

Blyth, A., Napolitano, R., & Glisic, B. (2019). Documentation, structural health monitoring, and numerical modeling for damage assessment of the Morris Island Lighthouse under environmental loading. *Philosophical Transactions of the Royal Society*. https://doi.org/10.1098/RSTA.2019.0002

Bosiljkov, V., Uranjek, M., Žarnić, R., & Bokan-Bosiljkov, V. (2010). An integrated diagnostic approach for the assessment of historic masonry structures. *Journal of Cultural Heritage*, *11*(3), 239–249.

Box, G. E. (1979). Robustness in the strategy of scientific model building. In R. L. Launer & G. N. Wilkinson (Eds.), *Robustness in statistics* (pp. 201–236). Amsterdam: Elsevier.

Bui, T., Limam, A., Sarhosis, V., & Hjiaj, M. (2017). Discrete element modelling of the in-plane and out-of-plane behaviour of dry-joint masonry wall constructions. *Engineering Structures*, *136*(2017), 277–294.

Burnham, K. P., & Anderson, D. R. (2004). Multimodel inference: Understanding AIC and BIC in model selection. *Sociological Methods & Research*, *33*(2), 261–304.

Chamberlin, T. C. (1992). Studies for students: The method of multiple working hypotheses. *Journal of Nutritional Medicine*, *3*(2), 159–165.

Cundall, P., & Hart, R. (2015). *Theory and background:3dec 3 dimensional distinct element code* (Technical Report). Minneapolis, MN: Itasca Consulting Group.

Douglas, I., Napolitano, R., Garlock, M., & Glisic, B. (2019). Reconsidering the vaulted forms of Cubas National School of Ballet. In R. Aguilar, D. Torrealva, S. Moreira, M. A. Pando, & L. F. Ramos (Eds.), *Structural analysis of historical constructions* (pp. 2150–2158). Berlin: Springer.

Elliott, L. P., & Brook, B. W. (2007). Revisiting Chamberlin: Multiple working hypotheses for the 21st century. *BioScience*, *57*(7), 608–614.

Fang, D. L., Napolitano, R. K., Michiels, T. L., & Adriaenssens, S. M. (2019). Assessing the stability of unreinforced masonry arches and vaults: A comparison of analytical and numerical strategies. *International Journal of Architectural Heritage*, *13*, 648–662.

Flamary, R., & Courty, N. (2017). *POT Python Optimal Transport library*. GitHub: https://github.com/rflamary/POT.

Gentile, C., & Saisi, A. (2007). Ambient vibration testing of historic masonry towers for structural identification and damage assessment. *Construction and Building Materials*, *21*(6), 1311–1321.

Giamundo, V., Sarhosis, V., Lignola, G., Sheng, Y., & Manfredi, G. (2014). Evaluation of different computational modelling strategies for the analysis of low strength masonry structures. *Engineering Structures*, *73*, 160–169.

Giordano, A., Mele, E., & De Luca, A. (2002). Modelling of historical masonry structures: Comparison of different approaches through a case study. *Engineering Structures*, *24*(8), 1057–1069.

Harris, S. Y. (2001). *Building pathology: Deterioration, diagnostics, and intervention*. Hoboken, NJ: John Wiley & Sons.

Kavanaugh, C., Morris, I. M., Napolitano, R., & Jorquera-Lucerga, J. J. (2017). Validating the use of graphical thrust line analysis for pier buttresses: The case study of Amiens Cathedral. *International Journal of Architectural Heritage*, *11*(6), 859–870.

Langston, C. (2012). Validation of the adaptive reuse potential (ARP) model using iconCUR. *Facilities*, *30*(3/4), 105–123.

Langston, C. A. (2010). Green adaptive reuse: Issues and strategies for the built environment. *International Conference on Sustainable Construction & Risk Management* (1165–1173). Chongqing Jiaotong University.

Langston, Y. L., & Langston, C. (2008). Reliability of building embodied energy modelling: An analysis of 30 Melbourne case studies. *Construction Management and Economics*, *26*(2), 147–160.

Lemos, J. (1998). Discrete element modelling of the seismic behaviour of stone masonry arches. *Computer Methods in Structural Masonry*, *4*, 220–227.

Lemos, J. V. (2007). Discrete element modeling of masonry structures. *International Journal of Architectural Heritage*, *1*(2), 190–213.

Lemos, J. V. (2019). Discrete element modeling of the seismic behavior of masonry construction. *Buildings*, *9*(2), 43.

Lourenço, P. B. (2002). Computations on historic masonry structures. *Progress in Structural Engineering and Materials*, *4*(3), 301–319.

Lupu, N., Selios, L., & Warner, Z. (2017). A new measure of congruence: The earth movers distance. *Political Analysis*, *25*(1), 95–113.

Merlino, K. R. (2018). *Building reuse: Sustainability, preservation, and the value of design*. Seattle, WA: University of Washington Press.

Michiels, T., Napolitano, R., Adriaenssens, S., & Glisic, B. (2017). Comparison of thrust line analysis, limit state analysis and distinct element modeling to predict the collapse load and collapse mechanism of a rammed earth arch. *Engineering Structures*, *148*, 145–156.

Milani, G., Valente, M., & Alessandri, C. (2017). The narthex of the Church of the Nativity in Bethlehem: A non-linear finite element

approach to predict the structural damage. *Computers & Structures*, *207*, 3–18.

Najafgholipour, M., Maheri, M. R., & Lourenço, P. B. (2013). Capacity interaction in brick masonry under simultaneous in-plane and out-of-plane loads. *Construction and Building Materials*, *38*, 619–626.

Napolitano, R., & Glisic, B. (2019a). Methodology for diagnosing crack patterns in masonry structures using photogrammetry and distinct element modeling. *Engineering Structures*, *181*, 519–528.

Napolitano, R., & Glisic, B. (2019b). Understanding the function of bonding courses in masonry construction: An investigation with mixed numerical methods. *Journal of Cultural Heritage*, *39*, 120–129.

Napolitano, R., Hess, M., Coe-Scharff, R., & Glisic, B. (2019). Numerical modeling of crack propagation in masonry structures. In R. Aguilar, D. Torrealva, S. Moreira, M. A. Pando, & L. F. Ramos (Eds.), *Structural analysis of historical constructions* (pp. 826–834). Berlin: Springer.

Napolitano, R., Hess, M., & Glisic, B. (2019a). Integrating non-destructive testing, laser scanning, and numerical modeling for damage assessment: The room of the elements. *Heritage*, *2*(1), 151–168.

Napolitano, R., Hess, M., & Glisic, B. (2019b). Quantifying the differences in documentation and modeling levels for building pathology and diagnostics. *Archives of Computational Methods in Engineering*. https//doi.org.10.1007/s11831-019-09350-y

Napolitano, R., Lansing, L., & Glisic, B. (2019). Understanding the function of Roman bonding courses: A numerical approach. In R. Aguilar, D. Torrealva, S. Moreira, M. A. Pando, & L. F. Ramos (Eds.), *Structural analysis of historical constructions* (pp. 1798–1806). Berlin: Springer.

Napolitano, R. K., & Glisic, B. (2018). Minimizing the adverse effects of bias and low repeatability precision in photogrammetry software through statistical analysis. *Journal of Cultural Heritage*, *31*, 46–52.

Napolitano, R. K., Hess, M., & Glisic, B. (2019c). The foundation walls of the Baptistery Di San Giovanni: A combination of laser scanning and finite-distinct element modeling to ascertain damage origins. *International Journal of Architectural Heritage*, *13*, 1180–1193.

Papantonopoulos, C., Psycharis, I., Papastamatiou, D., Lemos, J., & Mouzakis, H. (2002). Numerical prediction of the earthquake response of classical columns using the distinct element method. *Earthquake Engineering & Structural Dynamics*, *31*(9), 1699–1717.

Patias, P., Kaimaris, D., Georgiadis, C., Stamnas, A., Antoniadis, D., & Papadimitrakis, D. (2013). 3D mapping of cultural heritage: Special problems and best practices in extreme case-studies. *ISPRS Annals of Photogrammetry, Remote Sensing & Spatial Information Sciences II-5 (W1)*, 223–228.

Ramos, L. F., & Lourenço, P. B. (2004). Modeling and vulnerability of historical city centers in seismic areas: A case study in Lisbon. *Engineering Structures*, *26*(9), 1295–1310.

Rubner, Y., Tomasi, C., & Guibas, L. J. (2000). The earth mover's distance as a metric for image retrieval. *International Journal of Computer Vision*, *40*(2), 99–121.

Russo, S. (2013). Testing and modelling of dynamic out-of-plane behaviour of the historic masonry façade of Palazzo Ducale in Venice, Italy. *Engineering Structures*, *46*, 130–139.

Sarhosis, V., Garrity, S., & Sheng, Y. (2015). Influence of brick–mortar interface on the mechanical behaviour of low bond strength masonry brickwork lintels. *Engineering Structures*, *88*, 1–11.

Sarhosis, V., Tsavdaridis, K., & Giannopoulos, I. (2014). Discrete element modelling (DEM) for masonry infilled steel frames with multiple window openings subjected to lateral load variations. *Open Construction and Building Technology Journal*, *8*, 93–103.

Shrestha, S., Reina Ortiz, M., Gutland, M., Napolitano, R., Morris, I., Santana Quintero, M., … Maharjan, D. K. (2017). Digital recording and non-destructive techniques for the understanding of structural performance for rehabilitating historic structures at the Kathmandu Valley after Gorkha Earthquake 2015. *ISPRS Annals of Photogrammetry, Remote Sensing & Spatial Information Sciences*, *4*, 243–250.

Taylor, J. (2005). An integrated approach to risk assessments and condition surveys. *Journal of the American Institute for Conservation*, *44*(2), 127–141.

Wan, H.-P., & Ren, W.-X. (2014). Parameter selection in finite-element-model updating by global sensitivity analysis using Gaussian process metamodel. *Journal of Structural Engineering*, *141*(6), 04014164.

Watt, D. S. (2009). *Building pathology: Principles and practice*. Hoboken, NJ: John Wiley & Sons.

Williams, C. K., & Rasmussen, C. E. (1996). Gaussian processes for regression. In M. C. Mozer, M. I. Jordan, & T. Petsche (Eds.), *Advances in neural information processing systems* (pp. 514–520).

Wood, R. L., Mohammadi, M. E., Barbosa, A. R., Abdulrahman, L., Soti, R., Kawan, C. K., … Olsen, M. J. (2017). Damage assessment and modeling of the five-tiered pagoda-style Nyatapola Temple. *Earthquake Spectra*, *33*(S1), S377–S384.

Xia, Z., & Tang, J. (2013). Characterization of dynamic response of structures with uncertainty by using Gaussian processes. *Journal of Vibration and Acoustics*, *135*(5), 051006.

Yilmaz, U. (2009). *The earth mover's distance*. Retrieved from: https://www.mathworks.com/matlabcentral/fileexchange/22962-the-earth-mover-s-distance

Zhou, L., Yan, G., & Ou, J. (2013). Response surface method based on radial basis functions for modeling large-scale structures in model updating. *Computer-Aided Civil and Infrastructure Engineering*, *28*(3), 210–226.

How to cite this article: Napolitano R, Glisic B. Hybrid physics-based modeling and data-driven method for diagnostics of masonry structures. *Comput Aided Civ Inf*. 2020;1–12. https://doi.org/10.1111/mice.12548